The Planetary Science Journal, 7:142 (11pp), 2026 June https://doi.org/10.3847/PSJ/ae6fa9
© 2026. The Author(s). Published by the American Astronomical Society.
OPEN ACCESS

Bulk Thermal Conductivity of Granular Aggregates: Decoupling Coordination Number and Porosity

Bhuvan Agrawal[1], Matthias Grott[1], Moritz Goldmann[2], Bastian Gundlach[2], Jürgen Blum[3], Carsten Güttler[2], Jörg Kollenberg[1], Jens Biele[4], and Ansgar Greshake[5]
[1] German Aerospace Center, Berlin, Germany; bhuvan.agrawal@dlr.de
[2] Universität Münster, Münster, Germany
[3] Technische Universität Braunschweig, Braunschweig, Germany
[4] German Aerospace Center, Cologne, Germany
[5] Museum für Naturkunde, Berlin, Germany
Received 2025 December 23; revised 2026 April 24; accepted 2026 May 16; published 2026 June 4

Abstract

Both internal evolution and orbital dynamics of asteroids are influenced by the thermal conductivity of their surface regolith and boulders, yet the microstructural factors that control it remain poorly constrained. In this study, we use numerical simulations based on the discrete element method to quantify how porosity ϕ and coordination number Z, the average number of grain contacts, jointly influence solid heat transport in granular aggregates such as asteroid boulders under vacuum conditions. Using a modified random ballistic deposition algorithm, we generate particle assemblies in which ϕ and Z vary independently in certain ranges, allowing us to isolate their respective effects on effective thermal conductivity. Our results suggest that effective thermal conductivity cannot be expressed solely as a function of porosity. Instead, it follows a decoupled power-law relation $F(Z, \phi)$ with a threshold coordination number $Z_c = 2$. The model captures variations up to a factor of three in conductivity at fixed porosity ($\phi = 0.70$) and up to a factor of two at constant coordination number ($Z = 3.0$). Aggregates with a given bulk thermal conductivity are compatible with relative porosities $\Delta\phi/\phi$ that can vary by 17%. Our findings demonstrate that, apart from the contact size between individual grains and their intrinsic conductivity, microstructural connectivity exerts independent control over heat transport. The resulting two-parameter framework bridges microscopic packing geometry with bulk thermal behavior, offering a physically grounded basis for interpreting asteroid boulder properties and microstructures from spacecraft and laboratory thermal data.

Unified Astronomy Thesaurus concepts: Asteroid surfaces (2209)

1. Introduction

The behavior and evolution of planetesimals, from the early solar nebula to the present-day solar system, are strongly influenced by the thermal properties of their constituents. At early stages, they govern the heat transport in granular dust aggregates formed from micron-sized grains in the solar nebula (S. Henke et al. 2013; S.-i. Sirono 2017). In protoplanetary disks, the radial drift of dust aggregates is affected by photophoresis, whose efficiency is strongly dependent on their thermal conductivity (G. Wurm & H. Haack 2009; C. Loesche & G. Wurm 2012). At later evolutionary stages, the near-surface temperature distribution of comets and asteroids is likewise controlled by the conductivity of the outermost layers (J. Blum et al. 2017; T. Okada et al. 2017).

Thermal conductivity also affects surface modification processes. For instance, regolith generation and material loss due to thermal fatigue depend on the way surface materials respond to cyclic heating and cooling (e.g., M. Delbo et al. 2014; M. Hamm et al. 2019; J. L. Molaro et al. 2020; M. Hamm et al. 2025). On longer timescales, it is a critical parameter to model asteroid cooling after the era of heating due to radioactive decay of short-lived elements (W. Neumann et al. 2021). Additionally, the evolution and perturbation of asteroid orbits due to the Yarkovsky effect, described by W. F. Bottke et al. (2006), are sensitive to their surface thermal inertia. The internal thermal evolution, on the other hand, is controlled by thermal diffusivity of the interior. Understanding the conductivity of granular aggregates is therefore fundamental to studying asteroids from protoplanetary disks to their current dynamical state.

The microstructure of granular aggregates is itself a product of their formation and evolutionary history. During this period, granular aggregates may undergo hot or cold pressing, leaving distinct microstructural fingerprints. Hot pressing, driven by internal radiogenic or impact heating, promotes sintering through grain boundary diffusion. The contacts grow sintering necks, which close pores and increase contact areas (W. Neumann et al. 2014; H.-P. Gail et al. 2015). Cold pressing, in contrast, results from mechanical rearrangement under low temperature (impact compaction, gravitational loading, or seismic shaking) and primarily increases particle packing density and coordination number, i.e., average number of neighbors per particle, while leaving individual contact areas relatively small and unchanged (Z. Zhang et al. 2022). The distinct formation pathways give rise to fundamentally different contact network architectures, even at comparable bulk densities.

Recent space missions, such as Hayabusa2 (e.g., T. Okada et al. 2020; M. Hamm et al. 2022; T. Nakamura et al. 2023; K. Otto et al. 2023) and OSIRIS-REx (e.g., J. Emery et al. 2014;

Original content from this work may be used under the terms of the Creative Commons Attribution 4.0 licence. Any further distribution of this work must maintain attribution to the author(s) and the title of the work, journal citation and DOI.

D. S. Lauretta et al. 2017; D. N. DellaGiustina et al. 2019; B. Rozitis et al. 2020, 2022), have provided unprecedented constraints on the thermal properties of asteroid surfaces through combined remote-sensing, in situ measurements and analysis of returned samples. Thermal inertia derived from these measurements has been used to infer bulk porosities of surface materials. Both asteroids exhibit anomalously low thermal inertia compared to consolidated terrestrial rocks and meteorites (e.g., M. Grott et al. 2019; T. Okada et al. 2020; M. Hamm et al. 2020, 2022; B. Rozitis et al. 2020, 2022).

Several competing hypotheses have been proposed to explain this low thermal inertia. These include a surface monolayer of millimeter- to centimeter-scale particles (A. Ryan et al. 2024), as well as subsurface fractures and cracks interrupting near-surface heat flow (C. M. Elder 2025; M. Hamm et al. 2025; A. J. Ryan et al. 2026). Alternatively, high microporosity of the boulders has been a widely invoked interpretation, with inferred porosities for Ryugu (M. Grott et al. 2019; T. Okada et al. 2020; M. Hamm et al. 2022) and Bennu (M. Hamm et al. 2020; B. Rozitis et al. 2020, 2022) suggesting a loosely consolidated granular structure of the boulders. These estimates along with other studies (e.g., M. Krause et al. 2011; G. J. Flynn et al. 2018), however, depend on the assumed relationship between porosity and thermal conductivity. Since microstructural parameters such as particle coordination and contact geometry cannot be directly measured in situ, interpreting remote-sensing thermal inertia estimates in terms of porosity remains uncertain.

Bridging the gap between observational constraints and the underlying material properties requires a physical model linking grain-level contact properties to bulk thermal behavior. The thermal inertia $\Gamma = \sqrt{\rho c_p k_{\rm eff}}$ is a bulk quantity integrating contributions from material density ρ, heat capacity c_p, and effective thermal conductivity $k_{\rm eff}$. While ρ and c_p can be constrained through sample analysis and meteorite analogs and $k_{\rm eff}$ can in principle be estimated from thermal inertia measurements, the microstructural state that results in the observed thermal inertia cannot be uniquely recovered from such observations alone. This is an inherently degenerate problem since distinct microstructural configurations can yield identical bulk conductivities, making the interpretation of thermal observations fundamentally ambiguous in terms of mechanical properties.

It is important to distinguish between *microporosity* and *macroporosity*, both of which influence the bulk thermal response of asteroid materials but show relevance at different physical scales. Macroporosity refers to voids between boulders and large particles in a rubble-pile structure or aggregate. It operates at millimeter to decameter scale and describes void spaces in between particles (e.g., T. Michikami et al. 2019; D. N. DellaGiustina et al. 2020; M. Grott et al. 2020; A. J. Ryan et al. 2026). Microporosity, in contrast, describes the pores and fractures within particles and boulders and thus operates at the grain level. It thus relates to submillimeter pore spaces within boulders (e.g., T. Yada et al. 2021; R. D. Hanna et al. 2022; D. S. Lauretta et al. 2024; A. J. Ryan et al. 2026).

At temperatures characteristic of asteroids such as Ryugu and Bennu (T. Okada et al. 2020; B. Rozitis et al. 2020), and for submillimeter pore spaces, radiative heat transfer across pores is negligible compared to solid conduction through particle contacts. This contrasts with studies of loose regolith composed of millimeter-to-centimeter-scale particles, where radiation across larger pores can become a significant or even dominant heat transfer mechanism (B. Gundlach & J. Blum 2013; N. Sakatani et al. 2017; A. J. Ryan et al. 2022). Our simulations focus explicitly on the microstructural submillimeter regime, modeling the thermal behavior of the solid matrix inside boulders rather than large-scale macroporous structures.

While porosity and coordination number are often treated as functionally linked, this assumption can break down when formation history matters. In granular systems, porosity ϕ describes the bulk volume fraction of voids, whereas average coordination number Z quantifies local connectivity, i.e., the average number of contacts per particle. In the highly porous regime relevant to protoplanetary dust aggregates, ballistic cluster–cluster aggregation (P. Meakin 1991) produces chain-like structures of particles with one to two contacts each. On the other hand, mechanically compressed packings at comparable void fractions develop denser, more branched networks (J. Blum & G. Wurm 2008). The collision history determines the porosity and contact structure simultaneously (S. Okuzumi et al. 2012), such that the final microstructural state cannot, in general, be reconstructed from ϕ alone. Sintering and local particle rearrangement further decouple the two quantities: neck formation by surface and grain boundary diffusion increases Z without necessarily causing macroscopic shrinkage or pore closure (T. Rasp et al. 2013). Recognizing and quantifying this independence is crucial, as heat transport depends not only on bulk density of material but also on the topology of thermal conduction pathways.

Studies by N. Sakatani et al. (2017) and S. Arakawa et al. (2019) present an explicit treatment of both coordination number and porosity in vacuum conditions relevant to asteroids. N. Sakatani et al. (2017) constructed an analytical model juxtaposed to thermal experiments with glass beads, treating Z via an empirical relation (M. Suzuki et al. 1980) and computing thermal conductivity using parallel and serial thermal resistances. S. Arakawa et al. (2019) employed discrete element method (DEM) simulations to compute Z and $k_{\rm eff}$ for compressed dust aggregates, deriving power-law dependences $Z(\phi)$ and $k_{\rm eff}(\phi, Z(\phi))$. However, both studies collapse Z onto ϕ, yielding conductivity models effectively dependent on porosity alone. This convergence underscores a fundamental limitation: treating Z as a ϕ-dependent variable obscures its independent role in thermal transport. Thus, the above models cannot capture the full range of microstructural states that arise from the different formation and evolutionary pathways described above.

Thermal measurements of boulders on Ryugu and Bennu reveal that microporosities are systematically elevated compared to carbonaceous chondrite materials in our meteorite collections, with the majority of boulders exhibiting values in the range of ∼30%–50% (e.g., M. Grott et al. 2019; T. Okada et al. 2020; B. Rozitis et al. 2020). A distinct and scientifically significant subset of boulders, however, displays anomalously high porosities exceeding 70%, approaching values typical of cometary nuclei (N. Sakatani et al. 2021; T. Okada et al. 2020). These high-porosity boulders are interpreted as being composed of primordial material that escaped compaction and sintering (N. Sakatani et al. 2021). It is precisely in this high-porosity regime, where contact networks are sparse and chain-

like, that the decoupling of ϕ and Z is most consequential. Small changes in contact topology at such packing fractions can produce large variations in effective thermal conductivity. To address this, our study decouples porosity and coordination number in numerical simulations, providing a framework to interpret thermal data from both measurements and observations.

We present a DEM-based numerical study demonstrating that aggregates with similar porosities can exhibit markedly different effective thermal conductivities due to variations in contact topology and sintering state. Our results show that current interpretations of asteroid thermal inertia are intrinsically degenerate. We study porous aggregates as random packings of monodisperse spherical particles, representative of the grain-scale microstructure within asteroid boulders, generating assemblies such that Z and ϕ can be varied independently. By systematically exploring the (Z, ϕ)-parameter space, we examine how conductivity behaves at constant Z and at constant ϕ. Section 2 details the numerical model, including particle assembly generation, heat transfer in the contact network, and the subsequent structural and thermal analyses. Section 3 presents the bulk thermal conductivity model in terms of (Z, ϕ), and Section 4 discusses the implications for C-type asteroid boulders.

2. Modeling

2.1. Particle Assembly Generation

To investigate how microstructure, i.e., coordination number and porosity, controls bulk thermal conductivity, we generated assemblies using a random ballistic deposition with rolling (RBDR) algorithm as developed by L. Klar et al. (2024). This enables us to produce homogeneous packings of monodisperse spheres representing the granular matrix of asteroid material. While RBDR can, in principle, be used to generate packings representing both regolith and boulders, we only consider boulders in the subsequent thermal simulations (described in Section 2.4).

In the classical RBD scheme, individual spherical particles are sequentially released into a computation domain. Each new particle descends vertically until its first contact with either an already-deposited particle or the domain floor. The new particle is fixed at this position. With this procedure, we can generate highly porous aggregates with porosities $\phi \approx 0.87$ and coordination number $Z \approx 2$.

To access a wider structural range, two modifications have been introduced by L. Klar et al. (2024). First, after an incoming particle makes its initial contact, it is rolled further down by increasing its polar angle up to a maximum additional angle $\theta_{\max}$. Rolling stops when either a third supporting sphere is encountered or $\theta_{\max}$ is reached. Varying $0^\circ \leqslant \theta_{\max} \leqslant 180^\circ$ controls the degree of local rearrangement, with larger values promoting denser contact networks and higher coordination numbers. We produce assemblies with coordination number in the range $2 \lesssim Z \lesssim 4$.

The second modification allows multiple rolling attempts in different azimuthal directions. Up to N_φ orientations are tested, and the particle is placed at the position that yields the largest additional roll. Increasing N_φ enables particles to explore deeper intersects in the packing and has a lesser effect on the coordination number and rather specifies the range of achievable porosities. A floor function is applied to N_φ in the implementation; thus, only integer values produce microstructurally distinct assemblies. With $1 \leqslant N_\varphi \leqslant 360$, any noninteger values are mapped to $\lfloor N_\varphi \rfloor$, such that the minimum effective value is $N_\varphi = 1$. We produce assemblies spanning $0.50 \lesssim \phi \lesssim 0.87$.

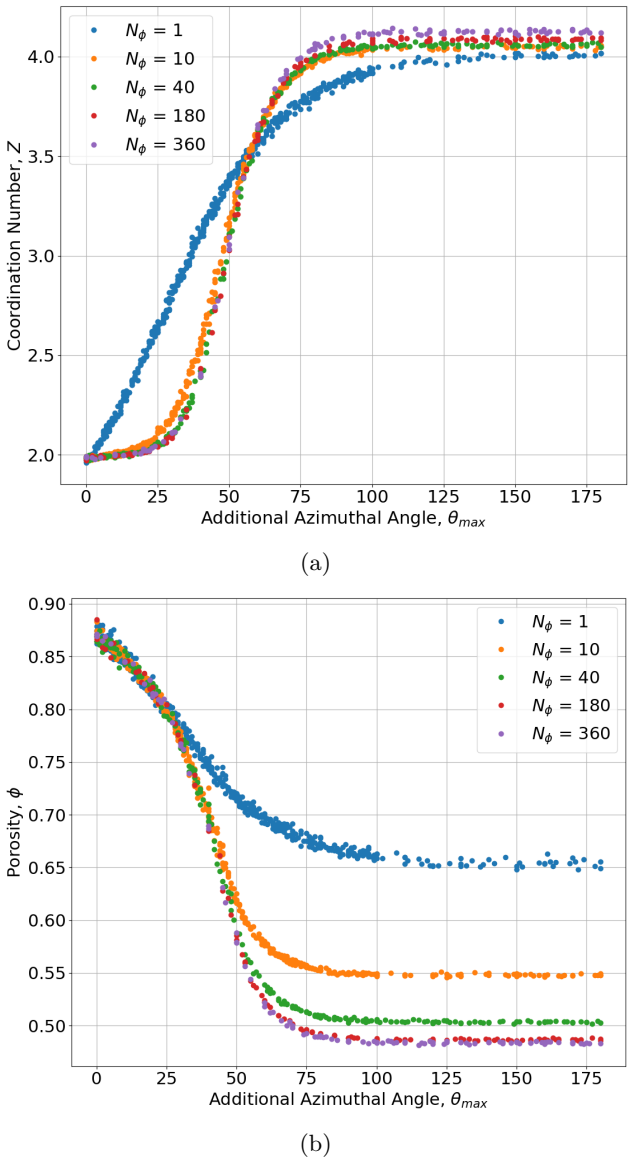

Figure 1. The variation of (a) coordination number and (b) porosity as a function of additional azimuthal angle $\theta_{\max}$ for different N_φ values (colored filled circles).

Figure 1 presents the extent of available parameter space, where the coordination number Z and porosity ϕ are presented as functions of azimuthal rolling angle $\theta_{\max}$ in Figures 1(a) and (b), respectively. It can be seen that while $\theta_{\max}$ strongly affects the coordination number, N_φ has lesser effect on it and rather specifies the range of achievable porosity.

The ($\theta_{\max}$, N_φ)-parameter control on the (Z, ϕ)-microstructural state provided by the RBDR algorithm allows us to generate assemblies with similar porosity but different coordination numbers, or vice versa, effectively decoupling the two parameters. Figure 2 shows representative examples of the granular assemblies produced using RBDR. We produce a range of microstructural states accessible with the algorithm.

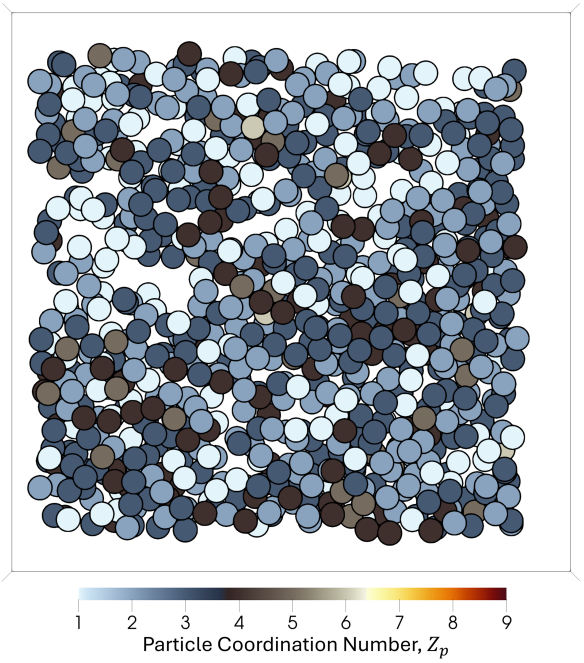

(a)

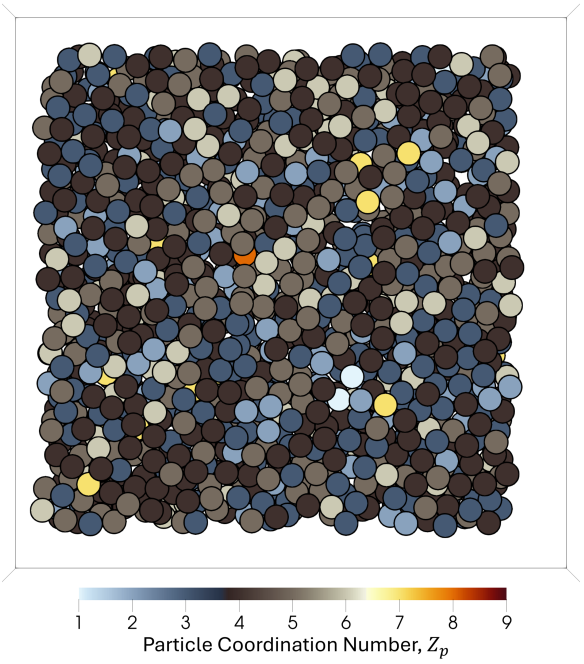

(b)

Figure 2. Cross-sectional layers of two different particle assemblies shown in panels (a) and (b) generated using the RBDR algorithm. The layer in panel (a) is taken from a highly porous particle aggregate with average coordination number $Z = 2.51$ and porosity $\phi = 0.67$, and panel (b) is a layer from a tightly packed aggregate with $Z = 4.05$ and $\phi = 0.49$. The color bars here denote the coordination number of individual particles.

Figures 2(a) and (b) present cross-sectional slices through low- and high-porosity assemblies, respectively. The cross-sectional views showcase the difference between the high- and low-porosity assemblies, with the former having much larger void spaces between particles. The coordination number of each particle, shown with the color bars, increases with a decrease in porosity.

We use the RBDR algorithm as implemented by L. Klar et al. (2024) to produce the particle assemblies, which are then imported into an open-source DEM code for thermal simulations discussed next. While the DEM code can perform the kinematics and dynamics calculations self-consistently, for the purposes of this study we exclude the mechanical evolution of the particle assemblies. Rather, after generating each packing with the RBDR algorithm, the particle positions are held fixed during the thermal simulations by disabling all mechanical force calculations. This ensures that the microstructure used to evaluate heat transfer remains identical to the one prescribed by the generation process. By constraining the particles in place, we isolate the thermal conduction problem from mechanical rearrangement effects and focus solely on how the prescribed contact network and packing geometry determine the effective thermal conductivity.

2.2. Heat Transport

For airless bodies such as asteroids, heat transport occurs through particle–particle contacts and radiative exchange within pore spaces. T. Nakamura et al. (2023) show that boulders on C-type asteroids are mainly composed of fine-grained matrix material with a few larger calcium-aluminum-rich inclusions or chondrules. According to N. Sakatani et al. (2017), at temperatures relevant for C-type asteroids, radiative transport starts to become important at particle radii larger than 100 μm, much larger than the particles in the fine-grained matrix of carbonaceous chondrites. Radiative heat transfer through pore spaces can therefore be neglected, and DEM can be used to model the heat transport. We study thermal conductivity of boulders on C-type asteroids using DEM numerical simulations and represent them as sintered aggregates of monodisperse spherical particles.

The thermal simulations are carried out using the Large-scale Atomic/Molecular Massively Parallel Simulator for Granular Materials (LIGGGHTS; C. Kloss et al. 2012), an open-source DEM code. For the heat transfer, LIGGGHTS extends the classical DEM framework by assigning each particle a temperature T_i. Heat transfer between particles i and j occurs through their contact point, with the heat transfer coefficient $h_{c,ij}$ determined by the contact area $A_{c,ij}$ between particles and their intrinsic thermal conductivities k_i and k_j. This is discussed is detail by M. G. Cooper et al. (1969) and given as

$$h_{c,ij} = 4\left(\frac{k_i\, k_j}{k_i + k_j}\right)\sqrt{\frac{A_{c,ij}}{\pi}}. \tag{1}$$

For the monodisperse assemblies in this study, we set $k_i = k_j = k_m$, as we consider identical spheres with material thermal conductivity k_m. Equation (1) thus reduces to $h_{c,ij} = 2k_m r_{c,ij}$, where $r_{c,ij} = \sqrt{A_{c,ij}/\pi}$ denotes the radius of contact between particles i and j.

Treatment of particle–particle contacts is a key consideration for modeling thermal conductivity. In asteroid boulders, the contact area between grains is controlled by microstructural effects such as surface roughness and sintering of contact asperities (e.g., B. N. J. Persson & J. Biele 2022). These processes modify the contact area and make the effective thermal conductance of a contact differ from what the Hertzian theory would predict. Rather than explicitly modeling neck growth, plastic deformation, or asperity-scale physics, we

prescribe a fixed thermal conductance for all particle–particle contacts. This approach represents the effective outcome of microphysical contact strengthening by the aforementioned mechanisms by imposing a finite and enhanced thermal bridge between grains. In this manner, it acts as a proxy for unresolved contact-scale processes while keeping the bulk geometry unchanged. By maintaining a constant contact conductance, we decouple bulk geometry from contact microphysics, allowing us to isolate the roles of coordination number and porosity in controlling bulk thermal conductivity.

In the absence of any heat generation due to sources (e.g., chemical reactions or radiative decays), the temperature change of particle i with mass m_i and specific heat capacity $c_{p,i}$ with each time step dt is given by the heat equation

$$m_i c_{p,i} \frac{dT_i}{dt} = q_i, \tag{2}$$

where the net heat flux into or out of the particle q_i is given by summing over the contributions from all its neighbors j as

$$q_i = \sum_j h_{c,ij}(T_j - T_i). \tag{3}$$

In this way, we compute bulk thermal transport in the contact network.

2.3. Coordination Number and Porosity

To quantify the geometric state of each particle assembly produced by the RBDR algorithm, we calculate two key microstructural parameters: coordination number Z, and porosity ϕ. The coordination number Z for a particle assembly is defined as the average number of contacts per particle. For each sphere, the number of neighbors is determined from the DEM contact list generated dynamically by LIGGGHTS. For both thermal modeling and geometrical calculations, two spheres are counted as being in contact if their center-to-center separation is at most $1.00035d_p$, where d_p is the particle diameter. This tolerance is introduced to account for numerical round-off errors in the contact detection algorithm and, as verified in our numerical experiments, yields a numerically robust coordination number that varies by less than a percent with respect to small perturbations in the tolerance value.

Particles located on the outermost faces of the assembly systematically possess fewer neighbors and thus can exhibit a coordination number as low as 1. The interior particles can have as many as nine neighbors as can be seen in Figure 2. To avoid artificially lowering the measured average coordination number, we therefore exclude the outermost particles and compute Z only from particles residing within the bulk of the assembly. The assembly-wide coordination number is then obtained by averaging the coordination number of all remaining bulk particles.

Porosity ϕ is defined as the fraction of void space within the cubic simulation domain,

$$\phi = 1 - \frac{V_{\text{occ}}}{V_{\text{tot}}}, \tag{4}$$

where V_{occ} is the total volume occupied by all the particles and V_{tot} is the volume of the cubic domain. We estimate the porosity of an assembly by randomly sampling points within the bounding computational domain. Using a Monte Carlo approach, we check whether each sampled point lies inside any of the spheres. The fraction of points inside the spheres gives the solid volume fraction ($V_{\text{occ}}/V_{\text{tot}}$), which is then used in Equation (4) to calculate ϕ. The number of sampled points is chosen such that the calculated porosity has a variation of less than $1/10$ of a percent.

In practice, both Z and ϕ are calculated after the assembly generation step and remain fixed during thermal simulations, since particles are mechanically constrained in place (Section 2.2). By analyzing Z and ϕ together, we construct a two-dimensional microstructural space in which to interpret bulk thermal conductivity results. This representation is essential for the independent study of packing density and interparticle connectivity.

2.4. Bulk Thermal Conductivity

To determine the effective bulk thermal conductivity of the assemblies, we simulate heat transport under steady-state flux boundary conditions. The cubic computational domain is bounded by two parallel faces, which are assigned equal but opposite heat fluxes, while all remaining boundaries are adiabatic. This setup, shown in Figure 3(a), establishes a global unidirectional heat flow across the assembly once thermal equilibrium is acquired as shown in Figure 3(b).

Each simulation advances through 9×10^8 computational time steps at a fixed step size of $\Delta t = 5$ μs, corresponding to a total simulated physical duration of 4500 s per run. In practice, each simulation requires approximately 2 days of wall-clock time to reach thermal equilibrium, though this varies with the computational resources allocated and the specific simulation setup. Thermal equilibrium is verified by two complementary checks. First, the net heat flux is computed across layers that are successive uniform cross sections perpendicular to the heat flow direction. This must tend to zero since energy conservation under true steady-state conditions requires it to be invariant throughout the bulk. Second, the input flux at each layer is compared against the flux imposed by boundary conditions. Post-processing and bulk conductivity analysis proceeds only if the relative difference between the two is within a percent, ensuring a physically consistent thermal equilibrium steady state.

Since particles in the outermost faces of the domain have lower coordination numbers, this artificially lowers the heat flux in those regions. Furthermore, imposed flux boundary conditions only affect the outer three to four particle layers at either end (see Figure 3(a)). To minimize these combined biases, we exclude a boundary layer of thickness approximately $5d_p$ from each face during post-processing. This scale ensures that the central bulk region of the assembly, where all calculations are performed, behaves as an infinite packing and is not dominated by boundary or imposed-flux artifacts. We ensure that the measured thermal properties are representative of the granular medium rather than the finite simulation box.

For the post-processing analysis, the bulk region is divided by $n + 1$ planes perpendicular to the global heat flow direction and separated by a distance of $1.05d_p$. The region between two consecutive planes forms a slice, and the particles with centers within each slice are together defined as a layer of particles denoted by subscript ℓ. A layer thickness of $1.05d_p$ ensures that each layer contains a statistically representative number of particles and contacts while still providing sufficient spatial resolution to resolve the macroscopic temperature gradient (described below).

In this manner, we divide the bulk into n layers of particles; see Figure 3(c). The net heat flux through a given layer is

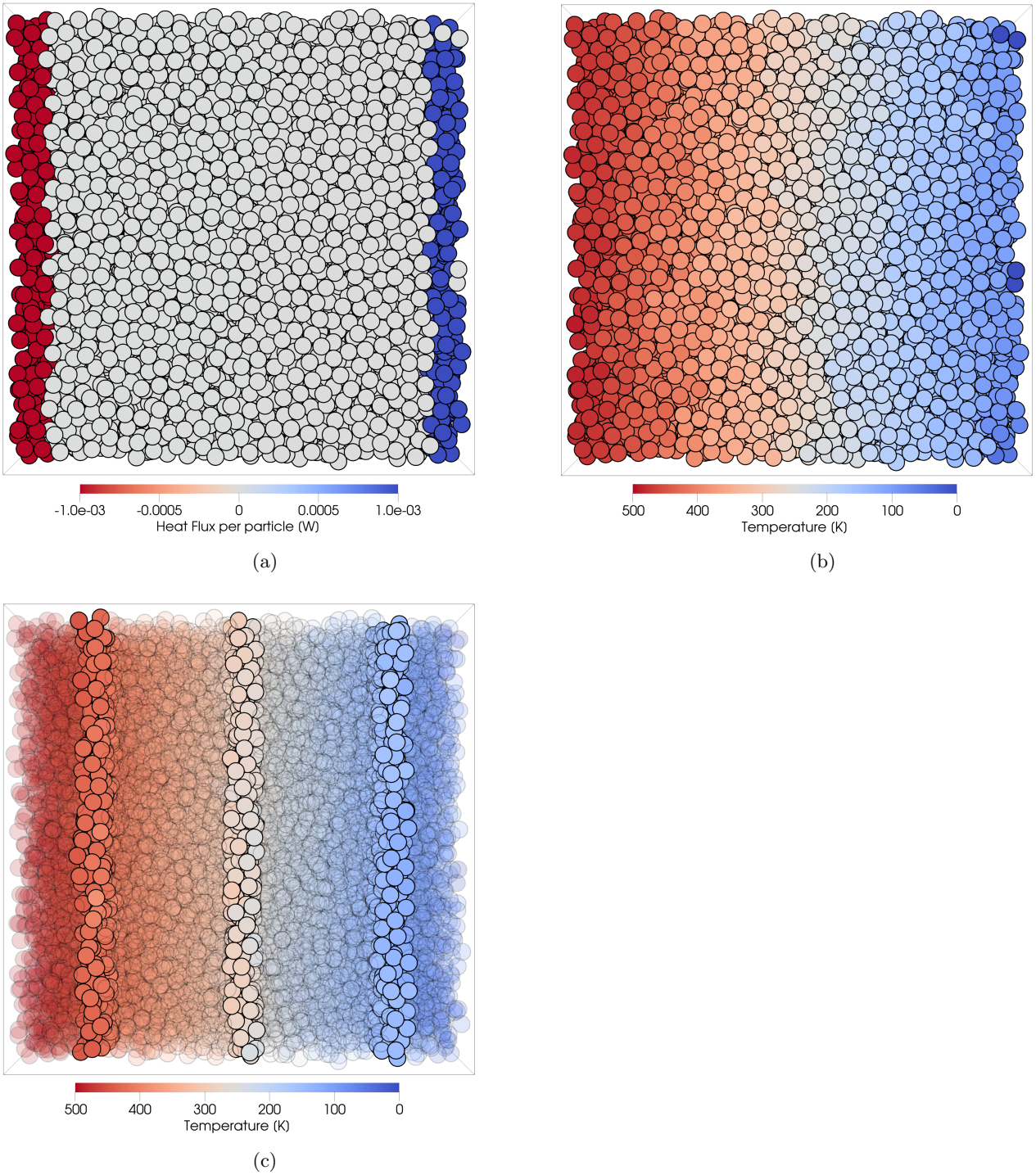

Figure 3. Numerical framework for the thermal simulations and post-processing pipeline. (a) The flux boundary conditions imposed while setting up the thermal simulations. The heat source and sink particles are shown in red and blue, respectively. Panels (b) and (c) show the same assembly in thermal equilibrium, with the color bar representing the equilibrium temperature of the particles. The three highlighted segments of the assembly in panel (c) are layers as described in Section 2.4. The entire assembly is sectioned into layers, but we only show three here for clarity.

calculated by summing the contributions of its constituent particles. For particle i in layer ℓ, the flux exchanged with a contacting neighbor j is $h_{c,ij}(T_j - T_i)$. The average flux density across the layer is then obtained by summing over all neighbors as

$$Q_\ell = \frac{1}{A_\ell} \sum_{i \in \ell} q_i, \tag{5}$$

where A_ℓ is the cross-sectional area of the layer or slice. The average bulk flux density across the assembly is then given by

$$Q = \frac{1}{n} \sum_{\ell=1}^{n} Q_\ell. \tag{6}$$

The temperature field within the computational domain is evaluated in parallel. For each layer ℓ, we compute the mean

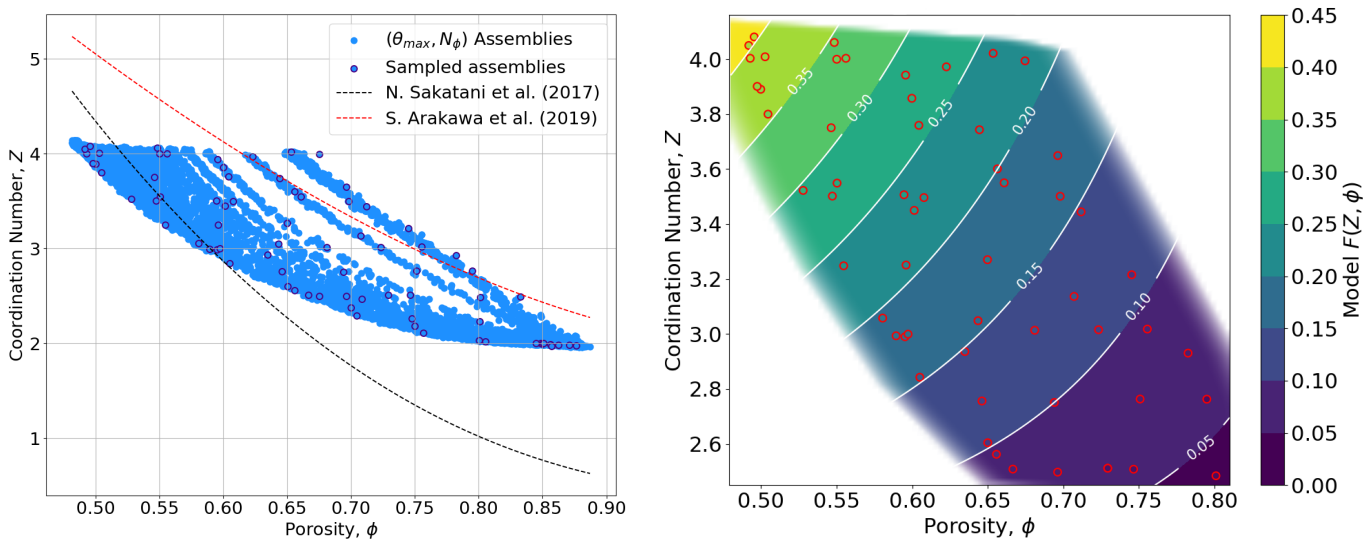

(a) (b)

Figure 4. (a) The (Z, ϕ)-parameter space, indicating the assemblies produced by RBDR with blue circles. The assemblies sampled for thermal simulations are highlighted here with a purple circle. The parameter spaces sampled by N. Sakatani et al. (2017) (dashed black) and S. Arakawa et al. (2019) (dashed red) are shown for reference. (b) Contours of dimensionless conductivity $F(Z, \phi)$ with respect to coordination number Z and porosity ϕ. The white lines are the constant conductivity isolines, and the color bar indicates the weighted least-squares best fit to simulation data. The red circles represent the particle assemblies in thermal equilibrium used for fitting.

particle temperature T_ℓ. By fitting the average layer temperature T_ℓ to their normalized positions z_ℓ along the direction of net heat flow, we obtain the macroscopic temperature gradient ∇T from the slope of the linear regression. We use the least-squares method to find the linear fit with the inverse of the standard deviation in T_ℓ as weights.

Finally, the effective bulk thermal conductivity is obtained using Fourier's law,

$$k_{\text{eff}} = -\frac{Q}{\nabla T}. \tag{7}$$

This procedure provides the effective thermal conductivity of the bulk of the particle assemblies. All calculations are carried out with fixed particle properties (radius, intrinsic material conductivity, contact radius, and heat capacity), so that variations in k_{eff} reflect only the effects of porosity and coordination number.

3. Results

3.1. Coordination Number–Porosity Relationship

We explore the (Z, ϕ)-parameter space using the RBDR algorithm and vary the deposition parameters $\theta_{\max}$ and N_φ to systematically study a broad range of packing structures. Together, the two controls generate a spread of assemblies that populate a broad range of (Z, ϕ)-parameter space as shown in Figure 4(a).

The gaps in the parameter space are a direct consequence of the discrete nature of rolling parameters ($\theta_{\max}$, N_φ). As detailed in Section 2.1, a floor function $\lfloor N_\varphi \rfloor$ in the implementation restricts its values to integers only. The rightmost gap, for example, therefore appears between $N_\varphi = 1$ and $N_\varphi = 2$, as any intermediate fractional value collapses to $N_\varphi = 1$, leaving the gap inaccessible.

A general trend of decreasing coordination number with increasing porosity is evident, along with the coupled influence of both deposition parameters on the resulting microstructure. The data, however, exhibit significant scatter. Depending on the deposition parameter set ($\theta_{\max}$, N_φ), assemblies at comparable porosities can demonstrate coordination numbers differing by up to $\Delta Z \sim 1.5$. Similarly, assemblies with comparable coordination numbers can span porosity ranges of up to $\Delta\phi \sim 0.17$. This scatter reflects that different rolling and settling pathways generate structurally distinct networks, with variations in local contact orientation and connectivity.

This nonunique relation contrasts with earlier models by N. Sakatani et al. (2017) and S. Arakawa et al. (2019), which treat Z as a deterministic function of ϕ, simplifying the microphysics considerably. Our results demonstrate that aggregates with the same porosity can be supported by markedly different contact networks, potentially resulting in different thermal transport properties. It is worth noting that this effect is strongest when considering large porosities, while the degeneracy is lifted for porosities below 0.50.

3.2. Thermal Conductivity Trends

We generated approximately 10,300 assemblies using RBDR. Thermal simulations were, however, run on a smaller subset. We selected a representative set of 76 assemblies from the available (Z, ϕ)-parameter space, chosen to provide systematic and approximately uniform coverage across the full range of coordination numbers and porosities. These are marked in Figure 4(a) with purple circles. These monodisperse particle assemblies span porosities $0.50 \lesssim \phi \lesssim 0.87$ and coordination numbers $2 \lesssim Z \lesssim 4$.

Among the 76 particle assemblies that were put through thermal simulations, those with $Z \lesssim 2.5$ were not able to reach a stable thermal equilibrium. We removed such nonequilibrium assemblies from further analysis (see below).

It is worth emphasizing that the model presented in Section 2.4 only considers purely conductive heat transfer via particle contacts. For $r_c/r_p \ll 1$, where r_p is the particle radius and r_c is the particle–particle contact radius, the heat

flux through a contact is proportional to the material thermal conductivity k_m and r_c (W. Siu & S.-K. Lee 2000). Consequently, the effective bulk thermal conductivities $k_{\rm eff}$ obtained from our simulations inherit the same dependencies. To isolate the structural influence of coordination number and porosity, it is convenient to normalize the conductivity by a characteristic contact scale.

The explicit dependence on material properties and contact radius is removed by normalizing the effective conductivity by the factor $(2k_m r_c/r_p)$. The resulting dimensionless conductivity is then given by

$$\frac{k_{\rm eff}}{\left(2k_m \frac{r_c}{r_p}\right)} \equiv F(Z, \phi). \tag{8}$$

In contrast to previous models (N. Sakatani et al. 2017; S. Arakawa et al. 2019), we retain both coordination number Z and porosity ϕ as independent structural variables. We find that their combined influence on heat transport is captured by a decoupled power law with coordination cutoff as

$$F(Z, \phi) = \begin{cases} A(Z - Z_c)^{\alpha} \ (1 - \phi)^{\beta}, & \text{for } Z > Z_c \\ 0, & \text{otherwise}, \end{cases} \tag{9}$$

where A, α, and β are positive constants and Z_c represents the critical coordination number below which the contact network fails to conduct.

Following S. Arakawa et al. (2019), we fix the cutoff at $Z_c = 2$. This corresponds to the minimum connectivity required for particles to contribute to a global solid network forming uninterrupted conductive chains. Below $Z_c = 2$, conductive pathways will remain highly fragmented, and no continuous heat-carrying backbone forms across the assembly.

This representation provides two practical advantages. First, it enables direct comparison between our results and earlier theoretical and experimental studies, regardless of the chosen material parameters. Second, it allows users of our model to reconstruct effective bulk thermal conductivity for their systems by selecting appropriate values of k_m and r_p. One can, in principle, also use different contact models, for example, the JKR theory, to obtain a physical basis for r_c/r_p. This, however, is not the focus of the current study. Specifically, once $F(Z, \phi)$ is obtained from our simulations, the dimensional conductivity can be recovered by rearranging Equation (8) and solving for $k_{\rm eff}$. Such a normalized and dimensionless framework separates the universal structural dependence from material-specific properties, offering a versatile basis for application to different asteroid regolith, planetary bodies, and analog materials where our assumptions remain applicable.

We adopt the decoupled power-law model with a coordination number threshold (Equation (9)) to capture the trends in the dimensionless conductivity model. The weighted least-squares best-fit parameters and uncertainties are summarized in Table 1.

The best-fit model $F(Z, \phi)$ forms contours and isolines in our parameter space as shown in Figure 4(b). The contours indicate that distinct microstructural states can yield the same effective conductivity. Note that the red circles in Figure 4(b) highlight the set of simulations that reached equilibrium state and were considered for our analysis. Our framework offers a way to quantify the uncertainty introduced by explicitly including coordination number. We observe that at constant porosity, say, $\phi = 0.70$, the dimensionless bulk conductivity can vary by a factor of 3. We see a similar response when varying the porosity at constant coordination number. For example, at $Z = 3.0$, the dimensionless conductivity varies by a factor of 2.

Table 1
Best-fit Parameters for Decoupled Power Law (Equation (9)) with $Z_c = 2$, Obtained by Bootstrapping the Thermal Simulations over the (Z, ϕ)-parameter Space

Symbols	Parameters	Mean	Standard Deviation
A	Dimensionless prefactor	0.60	0.04
α	Coordination exponent	0.71	0.02
β	Porosity exponent	1.34	0.07

Note. The thermal simulations span the ranges $2.5 \lesssim Z \lesssim 4.0$ and $0.50 \lesssim \phi \lesssim 0.80$. The rms error of the fit is 0.011.

The degeneracy between porosity and coordination number becomes more evident when studying the contour plot along constant-Z or constant-ϕ lines. In Figure 5 we show $F(Z, \phi)$ isolated along these lines emphasizing independent control of coordination number and porosity. In Figure 5(a), we present the model along constant-ϕ lines with respect to coordination number. We observe a systematic increase in $F(Z, \phi)$ and consequently in bulk thermal conductivity $k_{\rm eff}$, as each additional particle contact provides a new conductive pathway. Similarly, Figure 5(b) shows the dimensionless conductivity along constant-Z lines with respect to porosity. $F(Z, \phi)$ decreases with increasing porosity. In general, the number of particle–particle contacts in a given volume, i.e., the contact density, increases as porosity decreases. In Figure 5(c) we plot the decoupled power-law fit against $F(Z, \phi)$ determined from the simulations, demonstrating the quality of the best fit.

We compare our model to N. Sakatani et al. (2017) and S. Arakawa et al. (2019). These bound our simulations marking the edge cases along constant-ϕ lines, as seen in Figure 5(a). Thermal conductivity of an aggregate can agree with either of the two models depending on the different packing and compaction histories. The constant-Z lines can be used to traverse the space between the two models while maintaining a fixed thermal conductivity. This is shown in Figure 5(b).

4. Discussion and Conclusions

In this study we employed DEM-based numerical simulations to investigate how the effective thermal conductivity of granular aggregates depends jointly on coordination number Z and porosity ϕ. Using the RBDR algorithm (L. Klar et al. 2024), we generated particle assemblies that span a wide range of (Z, ϕ)-parameter combinations. This allowed us to explicitly decouple their respective influences on heat conduction through particle–particle contacts.

The results reveal that thermal conductivity cannot be expressed solely as a function of porosity. Instead, it follows a decoupled power-law relation with a threshold coordination number $Z_c = 2$, capturing the combined influence of packing density and microstructural connectivity. This formulation is particularly important in the range of intermediate to high porosity ($0.50 \lesssim \phi \lesssim 0.80$), where the scatter in the Z–ϕ relationship is largest and a single-valued mapping between

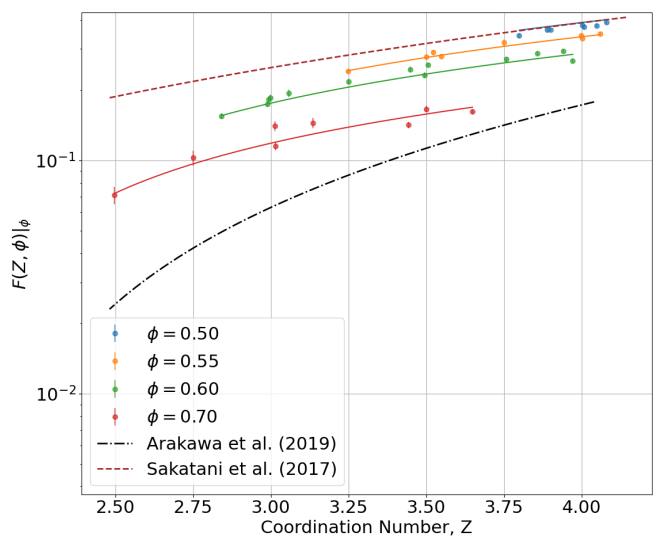

(a)

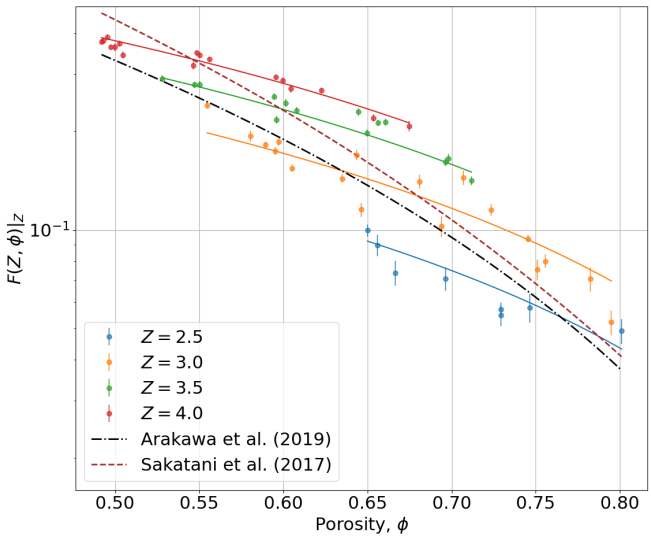

(b)

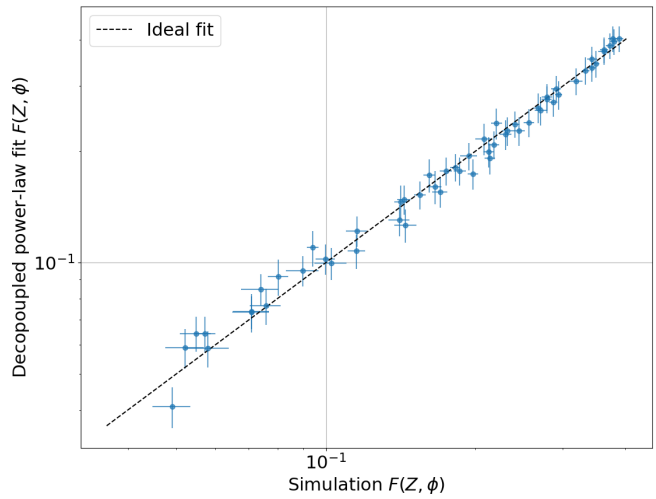

(c)

Figure 5. Best fit of the dimensionless bulk thermal conductivity as a function of coordination number Z and porosity ϕ. Panel (a) shows the behavior of the dimensionless function $F(Z, \phi)$ with respect to Z along constant-ϕ lines. The simulation results (filled circles) are fitted with the decoupled power-law Equation (9) (solid lines). Panel (b) is a similar plot along constant-Z lines, which are shown with different colored circles (simulations) and lines (model fit). We also compare our results with the same normalized bulk thermal conductivity from S. Arakawa et al. (2019) (dashed–dotted black line) and N. Sakatani et al. (2017) (dashed brown line). Panel (c) compares the decoupled power-law model fit with dimensionless conductivity from the simulations. The black dotted line here represents the ideal fit. Note that the error bars in the three panels represent one standard deviation on the parameters.

them is least justified. For $\phi > 0.80$, particle assemblies in our study have a coordination number $2.0 \lesssim Z \lesssim 2.5$. Due to a sparsely connected particle network, these assemblies were barely conducting and never reached a stable thermal equilibrium and thus were removed from model fitting and analysis.

The threshold coordination number $Z_c = 2$ marks the transition between disconnected and percolating contact networks. Below this critical value, the assemblies remain geometrically disconnected, lacking a continuous solid pathway linking the hot and cold boundaries. Consequently, heat transport remains strongly suppressed. Once Z exceeds Z_c, the system crosses a percolation threshold where a contiguous network of solid contacts links the boundaries, enabling bulk-scale conduction. The critical coordination number therefore defines the minimal structural connectivity required for sustained solid heat transport in granular aggregates. On average, each grain must establish at least two stable contacts to form part of a continuous conductive path.

The dependence of thermal conductivity on porosity arises from two complementary structural effects. First, at fixed coordination number, decreasing ϕ increases the contact density in the granular aggregates, thereby strengthening the global conductive network. Second, at fixed porosity, increasing Z adds auxiliary conduction paths per particle, lowering the overall thermal resistance of the aggregates. These two effects jointly define the density and excess of conduction pathways, explaining why both parameters must be included in a predictive model of granular heat transport.

In our DEM simulations, the contact radius r_c was held constant to isolate structural effects from contact-scale variations. In nature, however, r_c/r_p evolves with thermal

and mechanical history of the aggregate. Cold-pressing materials maintain small contact areas governed by asperities, whereas hot pressing or sintering enlarges the interparticle necks and increases r_c/r_p. Conversely, thermal fatigue or micrometeoroid bombardment can reduce these areas by introducing microcracks or roughness. These variations modify absolute conductivities, but our normalization effectively removes these dependencies, allowing $F(Z, \phi)$ to be flexibly applied for any physically plausible r_c/r_p, or more generally h_c/r_p.

Most existing models of heat transport in granular materials express bulk thermal conductivity primarily as a function of porosity. Both N. Sakatani et al. (2017) and S. Arakawa et al. (2019) formulate solid-network conductivity as a product of material and contact-scale terms, such as intrinsic grain conductivity k_m and normalized contact radius r_c/r_p, and a geometric factor $f(\phi)$. To simplify this dependence, both replace the microstructural degree of freedom Z with an empirical relation $Z(\phi)$, yielding a one-to-one mapping between porosity and conductivity. This assumption performs well at a limited parameter space but is no longer reliable at intermediate ϕ, where aggregates with identical porosity can exhibit distinct connectivity networks.

Our simulations quantify this limitation directly. In the intermediate-porosity regime ($0.50 \lesssim \phi \lesssim 0.80$), Z is not uniquely determined by ϕ. Assemblies with similar porosity can differ in coordination number depending on their deposition or formation histories, leading to substantial differences in conductivity even when k_m and r_c/r_p are fixed. We observe that at constant porosity, for example, $\phi = 0.70$, the dimensionless bulk conductivity can vary by a factor of three across assemblies with different coordination numbers. Similarly, at constant connectivity $Z = 3.0$, it can vary by a factor of two as porosity changes. According to our best-fit model $F(Z, \phi)$, such variations imply that two aggregates with identical measured conductivities could differ in porosity by as much as $\Delta\phi \approx 0.11$. This degeneracy introduces a nontrivial uncertainty in the interpretation of porosity from thermal measurements.

The parameter space explored here is bounded by the geometric and algorithmic limitations of the RBDR method. Our simulations cover $0.50 \lesssim \phi \lesssim 0.87$ and $2 \lesssim Z \lesssim 4$, leaving the low-ϕ, low-Z and high-ϕ, high-Z regions of parameter space unsampled. Extrapolations of our results beyond these limits should therefore be treated with caution. Not all (Z, ϕ) combinations are physically realizable for monodisperse, nonsintered spheres. At low porosity, dense packings with few contacts are mechanically unstable, forcing Z upward as particles are geometrically constrained. Conversely, highly porous structures cannot maintain large Z without reducing void space, since adding contacts necessarily lowers ϕ. These geometric constraints define the natural domain of validity for our conductive model. Achieving lower porosities ($\phi < 0.5$) would require either polydisperse packings or compaction, which are beyond the reach of the packing algorithm used.

The decoupled $F(Z, \phi)$ formulation is directly relevant to the interpretation of thermal measurements of carbonaceous chondrites and C-type asteroid boulders. Analysis of returned samples and in situ measurements from Hayabusa2 and OSIRIS-REx indicates that boulders on Ryugu and Bennu are fine grained and mechanically weak, with porosities that, while moderate in absolute terms, are elevated relative to the dense, chondritic material in our meteorite collections (M. Grott et al. 2019; T. Okada et al. 2020; B. Rozitis et al. 2020; T. Nakamura et al. 2023). Crucially, the relationship between effective thermal inertia and porosity is not unique, and multiple combinations of coordination number and void fraction can yield the same bulk conductivity. Our results show that variations in coordination number at fixed thermal conductivity can result in relative porosity uncertainty as high as 17%. This needs to be taken into account when estimating porosity from thermal measurements.

Although our simulations focus on monodisperse spherical particles representative of the fine-grained matrix within meteorites and boulders, several simplifications inherent to this idealization warrant future investigation. Irregular particle shapes, polydisperse size distributions, and evolving contact areas through sintering or fracturing are all factors that influence the thermal conduction network and are not captured by the present study. Furthermore, while radiative heat transfer across pore spaces is negligible for the fine-grained material ($r_p \lesssim 100\ \mu$m) and temperature regime ($T \lesssim 300$ K) considered here, this approximation may break down when considering larger grain sizes or elevated temperatures.

Under the limiting assumptions stated above, the microphysical principles established in this study extend to rubble-pile structures as well. In those macroscopic, polydisperse packings, the Z–ϕ relationship will be more complex, but the dual control of contact density and connectivity on thermal conductivity is expected to persist. However, such scenarios are beyond the scope of the current work and remain to be studied in the future.

Acknowledgments

This work has been supported by the Deutsche Forschungsgemeinschaft (DFG) through contract GR 3751/2-1. We are grateful to our colleagues at TU Braunschweig and University of Münster for stimulating discussions and critical feedback during the research and development of this study. The authors gratefully acknowledge the scientific support and HPC resources provided by the German Aerospace Center (DLR). The HPC system CARA is partially funded by "Saxon State Ministry for Economic Affairs, Labour and Transport" and "Federal Ministry for Economic Affairs and Climate Action." We also acknowledge the use of the open-source DEM code LIGGGHTS.

The authors also acknowledge the use of AI-assisted language editing tools for grammar correction and improvements in clarity (OpenAI 2025). All AI-generated text was fully reviewed, verified, and revised by the authors. They also take complete responsibility for the development and execution of research design, simulations, data analysis, and scientific conclusions.

Software: LIGGGHTS (C. Kloss et al. 2012), ChatGPT (OpenAI 2025).

Author Contributions

The study was designed by B.A., M.G., and J.B. The scientific computations, numerical simulations, and data analysis were performed by B.A., who also wrote the initial draft manuscript. M.G., J.K., and J.B. provided guidance on the thermal modeling framework and assisted with interpretation of the results. M.G., J.B., and B.G. supervised the project

and, in collaboration with J.B., contributed to the theoretical framework. All the authors revised the manuscript, discussed the results, and contributed to the final version of the paper.

ORCID iDs

Jens Biele https://orcid.org/0000-0002-7414-829X

References

Arakawa, S., Tatsuuma, M., Sakatani, N., & Nakamoto, T. 2019, Thermal Conductivity and Coordination Number of Compressed Dust Aggregates, Icar, 324, 8

Blum, J., Gundlach, B., Krause, M., et al. 2017, Evidence for the Formation of Comet 67P/Churyumov-Gerasimenko through Gravitational Collapse of a Bound Clump of Pebbles, MNRAS, 469, S755

Blum, J., & Wurm, G. 2008, The Growth Mechanisms of Macroscopic Bodies in Protoplanetary Disks, ARA&A, 46, 21

Bottke, W. F., Vokrouhlický, D., Rubincam, D. P., & Nesvorný, D. 2006, The Yarkovsky and YORP Effects: Implications for Asteroid Dynamics, AREPS, 34, 157

Cooper, M. G., Mikic, B. B., & Yovanovich, M. M. 1969, Thermal Contact Conductance, IJHMT, 12, 279

Delbo, M., Libourel, G., Wilkerson, J., et al. 2014, Thermal Fatigue as the Origin of Regolith on Small Asteroids, Natur, 508, 233

DellaGiustina, D. N., Burke, K. N., Walsh, K. J., et al. 2020, Variations in Color and Reflectance on the Surface of Asteroid (101955) Bennu, Sci, 370, eabc3660

DellaGiustina, D. N., Emery, J. P., Golish, D. R., et al. 2019, Properties of Rubble-pile Asteroid (101955) Bennu from OSIRIS-REx Imaging and Thermal Analysis, NatAs, 3, 341

Elder, C. M. 2025, Boulders on Bennu: Low Apparent Thermal Inertia Caused by Thermal Fatigue Fractures, GeoRL, 52, e2025GL116256

Emery, J., Fernández, Y., Kelley, M., et al. 2014, Thermal Infrared Observations and Thermophysical Characterization of OSIRIS-REx Target Asteroid (101955) Bennu, Icar, 234, 17

Flynn, G. J., Consolmagno, G. J., Brown, P., & Macke, R. J. 2018, Physical Properties of the Stone Meteorites: Implications for the Properties of Their Parent Bodies, Geoch, 78, 269

Gail, H.-P., Henke, S., & Trieloff, M. 2015, A&A, 576, A60

Grott, M., Biele, J., Michel, P., et al. 2020, Macroporosity and Grain Density of Rubble Pile Asteroid (162173) Ryugu, JGRE, 125, e2020JE006519

Grott, M., Knollenberg, J., Hamm, M., et al. 2019, Low Thermal Conductivity Boulder with High Porosity Identified on C-Type Asteroid (162173) Ryugu, NatAs, 3, 971

Gundlach, B., & Blum, J. 2013, A New Method to Determine the Grain Size of Planetary Regolith, Icar, 223, 479

Hamm, M., Grott, M., Senshu, H., et al. 2022, Mid-infrared Emissivity of Partially Dehydrated Asteroid (162173) Ryugu Shows Strong Signs of Aqueous Alteration, NatCo, 13, 364

Hamm, M., Pelivan, I., Grott, M., & de Wiljes, J. 2020, Thermophysical Modelling and Parameter Estimation of Small Solar System Bodies via Data Assimilation, MNRAS, 496, 2776

Hamm, M., Senshu, H., & Grott, M. 2019, Latitudinal Dependence of Asteroid Regolith Formation by Thermal Fatigue, Icar, 319, 308

Hamm, M., Strauß, M., Grott, M., et al. 2025, Low Thermal Inertia of (162173) Ryugu a Result of Horizontal Cracks in Boulders, Icar, 430, 116484

Hanna, R. D., Ketcham, R. A., Edey, D. R., & O'Connell, J. 2022, 3D Porosity Structure of the Earliest Solar System Material, NatSR, 12, 8369

Henke, S., Gail, H.-P., Trieloff, M., & Schwarz, W. 2013, Thermal Evolution Model for the H Chondrite Asteroid-instantaneous Formation versus Protracted Accretion, Icar, 226, 212

Klar, L., Glißmann, T., Lammers, K., G´uttler, C., & Blum, J. 2024, Structural Properties of Different Sphere Packings with Arbitrary Porosities for Planetary-science Applications, GranM, 26, 59

Kloss, C., Goniva, C., Hager, A., Amberger, S., & Pirker, S. 2012, Model, Algorithms and Validation for Opensource DEM and CFD-DEM, Progress in Computational Fluid Dynamics, An International Journal, 12, 140

Krause, M., Henke, S., Gail, H.-P., et al. 2011, LPSC, 42, 2696

Lauretta, D. S., Balram-Knutson, S. S., Beshore, E., et al. 2017, OSIRIS-REx: Sample Return from Asteroid (101955) Bennu, SSRv, 212, 925

Lauretta, D. S., Connolly, H. C., Aebersold, J. E., et al. 2024, Asteroid (101955) Bennu in the Laboratory: Properties of the Sample Collected by OSIRIS-REx, M&PS, 59, 2453

Loesche, C., & Wurm, G. 2012, Theoretical and Photophoretic Properties of Dust Mantled chond444 and Sorting in the Solar Nebula, A&A, 545, A36

Meakin, P. 1991, Fractal Aggregates in Geophysics, RvGeo, 29, 317

Michikami, T., Honda, C., Miyamoto, H., et al. 2019, Boulder Size and Shape Distributions on Asteroid Ryugu, Icar, 331, 179

Molaro, J. L., Hergenrother, C. W., Chesley, S. R., et al. 2020, Thermal Fatigue as a Driving Mechanism for Activity on Asteroid Bennu, JGRE, 125, e2019JE006325

Nakamura, T., Matsumoto, M., Amano, K., et al. 2023, Formation and Evolution of Carbonaceous Asteroid Ryugu: Direct Evidence from Returned Samples, Sci, 379, eabn8671

Neumann, W., Breuer, D., & Spohn, T. 2014, Modelling of Compaction in Planetesimals, A&A, 567, A120

Neumann, W., Grott, M., Trieloff, M., et al. 2021, Microporosity and Parent Body of the Rubble-pile NEA (162173) Ryugu, Icar, 358, 114166

Okada, T., Fukuhara, T., Tanaka, S., et al. 2017, Thermal Infrared Imaging Experiments of C-Type Asteroid 162173 Ryugu on Hayabusa2, SSRv, 208, 255

Okada, T., Fukuhara, T., Tanaka, S., et al. 2020, Highly Porous Nature of a Primitive Asteroid Revealed by Thermal Imaging, Natur, 579, 518

Okuzumi, S., Tanaka, H., Kobayashi, H., & Wada, K. 2012, Rapid Coagulation of Porous Dust Aggregates outside the Snow Line: A Pathway to Successful Icy Planetesimal Formation, ApJ, 752, 106

OpenAI 2025, ChatGPT, https://chat.openai.com

Otto, K., Ho, T.-M., Ulamec, S., et al. 2023, MASCOT's In Situ Analysis of Asteroid Ryugu in the Context of Regolith Samples and Remote Sensing Data Returned by Hayabusa2, EP&S, 75, 51

Persson, B. N. J., & Biele, J. 2022, Heat Transfer in Granular Media with Weakly Interacting Particles, AIPA, 12, 105307

Rasp, T., Kraft, T., & Riedel, H. 2013, Discrete Element Study on the Influence of Initial Coordination Numbers on Sintering Behaviour, ScrMa, 69, 805

Rozitis, B., Ryan, A. J., Emery, J. P., et al. 2020, Asteroid (101955) Bennu's Weak Boulders and Thermally Anomalous Equator, SciA, 6, eabc3699

Rozitis, B., Ryan, A. J., Emery, J. P., et al. 2022, High-resolution Thermophysical Analysis of the OSIRIS-REx Sample Site and Three Other Regions of Interest on Bennu, JGRE, 127, e2021JE007153

Ryan, A., Rozitis, B., Pino Munoz, D., et al. 2024, Rocks with Extremely Low Thermal Inertia at the OSIRIS-REx Sample Site on Asteroid Bennu, PSJ, 5, 92

Ryan, A. J., Ballouz, R.-L., Macke, R. J., et al. 2026, Low Thermal Inertia of Carbonaceous Asteroid Bennu Driven by Cracks Observed in Returned Samples, NatCo, 17, 2443

Ryan, A. J., Pino Muñoz, D., Bernacki, M., et al. 2022, Full-field Modeling of Heat Transfer in Asteroid Regolith: 2. Effects of Porosity, JGRE, 127, e2022JE007191

Sakatani, N., Ogawa, K., Iijima, Y., et al. 2017, Thermal Conductivity Model for Powdered Materials under Vacuum Based on Experimental Studies, AIPA, 7, 015310

Sakatani, N., Tanaka, S., Okada, T., et al. 2021, Anomalously Porous Boulders on (162173) Ryugu as Primordial Materials from its Parent Body, NatAs, 5, 766

Sirono, S.-i. 2017, Heating of Porous Icy Dust Aggregates, ApJ, 842, 11

Siu, W., & Lee, S.-K. 2000, Effective Conductivity Computation of a Packed Bed Using Constriction Resistance and Contact Angle Effects, IJHMT, 43, 3917

Suzuki, M., Makino, K., Yamada, M., & Iinoya, K. 1980, A Study of Coordination Number in a Rondom Packed System of Monosized Sphere Particles, Kagaku Kogaku Ronbonshu, 6, 59

Wurm, G., & Haack, H. 2009, Outward Transport of CAIs during FU-Orionis Events, M&PS, 44, 689

Yada, T., Abe, M., Okada, T., et al. 2021, Preliminary Analysis of the Hayabusa2 Samples Returned from C-Type Asteroid Ryugu, NatAs, 6, 214

Zhang, Z., Bercovici, D., & Elkins-Tanton, L. 2022, Cold Compaction and Macro-porosity Removal in Rubble-pile Asteroids: 2. Applications, JGRE, 127, e2022JE007343